Authors' Accepted Manuscript - International Journal of Mechanical Sciences (2023)
https://doi.org/10.1016/j.ijmecsci.2023.108196

Multi-stability of the hexagonal origami hypar based on group theory and symmetry breaking

Yao Chen [a,*], Ruizhi Xu [a], Chenhao Lu [a], Ke Liu [b], Jian Feng [a], Pooya Sareh [c,d]

[a] *Key Laboratory of Concrete and Prestressed Concrete Structures of Ministry of Education, and National Prestress Engineering Research Center, Southeast University, Nanjing 211189, China*
[b] *Department of Advanced Manufacturing and Robotics, Peking University, Beijing 100871, China*
[c] *Creative Design Engineering Lab (Cdel), Department of Mechanical and Aerospace Engineering, School of Engineering, University of Liverpool, Liverpool, L69 3GH, UK*
[d] *Escuela Técnica Superior de Ingeniería y Diseño Industrial, Universidad Politécnica de Madrid (UPM), Madrid 28040, Spain*

Keywords:
Origami hypar
Multi-stability
Group theory
Bifurcation
Symmetry breaking

A B S T R A C T

The origami hyperbolic paraboloid, or the hypar, is widely known for its characteristic non-zero Gaussian curvature and multi-stable states. Previous investigations have mainly considered two particular cases of the origami hypar patterns, namely the square and the circular hypars. As a representative example of general polygonal hypar patterns, the hexagonal origami hypar displays more desirable energy properties and subtler multi-stable configurations, which is however, rarely studied. In this paper, we investigate the multi-stability of the hexagonal origami hypar by combining a group-theoretic approach, a symmetry-breaking method, and a bar-and-hinge structural model, to simplify the kinematic analysis of this highly symmetric structure . Notably, the kinematic path of the hexagonal origami hypar is divided into three bifurcation branches by symmetry breaking. Each branch corresponds to two symmetric stable states according to the equilibrium loading and potential energy simulated using the bar-and-hinge model. The non-rigid deformation of the hexagonal origami hypar is mainly controlled by the folding of creases and the bending of facets. Moreover, the energy barrier among the stable states becomes increasingly stronger with higher symmetry orders, thicker sheets of material, and longer creases. This work provides a new strategy for analyzing multi-stable origami structures with high symmetry orders, which can be useed in the design and development of novel adaptive or deployable engineering structures.

1. Introduction

Multi-stable systems possess non-trivial energy landscapes that lead to multiple distinct stable configurations. As a result of various desirable characteristics of such systems , in recent years, they have been increasingly adopted in bionics [1,2], metamaterials [3,4], robotics [5–8], engineering structures [9–11,85] and other fields. From a structural design viewpoint, many multi-stable systems are designed by combining bistable units [12]. In general, the local properties and method of combination of these units have a critical impact on the global properties of a multi-stable system. For example, a well-assembled double-layer Kresling tube can achieve the same total height in two different stable states [13]. The rich mechanics of origami structures provide many candidates for such bistable units and have been a main source of inspiration for the design of multi-stable structures, such as the Kresling configurations with different stable-state numbers [14], the Kresling assembly [15,16], and kirigami-based metastructures [17].

A number of multi-stable origami structures are derived from traditional origami patterns, such as the Miura-ori [18–31], Tachi-Miura polyhedron [32,33], Waterbomb tubes [34,35], and Kresling tubes [36,37]. By combining multi-stable origami units such as the square twist [38,39], leaf-like origami [40], origami-inspired cellular [41,42], and origami hypar [43], we can produce higher numbers of stable states and richer levels of programmability in designing origami structures. To ensure smooth deployment and transition processes, kinematic analysis is a key consideration in the design and analysis of multi-stable origami structures [44]. The existing methods for the kinematic analysis of rigid or non-rigid origami can be divided into two types: (1) mechanism analysis, and (2) structural analysis. In general, the conditions of rigid folding are more complex than those of non-rigid folding; therefore, the

* Corresponding author.
E-mail address: chenyao@seu.edu.cn (Y. Chen).

kinematic analysis of rigid folding is simpler and more campatible with a wide range of computational models [45]. Kinematics of rigid origami can be simulated by means of mechanism analysis methods such as polygonal surfaces [46] and spherical polygonal linkages [47], as well as by structural analysis methods such as the bar-and-hinge [48] and shell [49] models. However, non-rigid folding involves the deformations of origami facets, which greatly increase the variables to be considered [50]. Thus, in general, for non-rigid origami, mechanism analysis methods are not applicable to the study of non-rigid origami structures. The most common analytical methods for analyzing non-rigid origami structures are as follows: (1) the bar-and-hinge model with elastic bars for the tension and compression of facets and rotating springs for the bending of them [51,52]; (2) the membrane-and-hinge model with elastic membranes for the tension and compression of facets and rotating springs for the bending of them [53]; and (3) the thin plate elements model [54].

The origami hypar, as a non-rigid and multi-stable origami unit, is composed of concentrically pleated polygons with a minimum of four sides [55]. Among this family of patterns, two extreme cases have been widely studied, namely, the square origami hypar [56] and the circular origami hypar (note that a circle can be considered as a polygon with an infinite number of sides) [57,58]. The square origami hypar has two stable states that are macroscopically symmetric with a rotation of 90° [43]. When transitioning from one stable state to the other, it first unfolds to a flat state and then refolds up, going through a significant energy barrier caused by the competing folding, bending, and stretching energies [51]. Moreover, the folding angle of the square origami hypar can be regulated by controlling the defects of creases [59]to make the structure reach the appropriate stable state. On the other hand, the circular origami hypar can reach different stable states under certain approximate conditions [60]; in the simplest condition, it forms a saddle-like shape. Nevertheless, except for these two extreme cases, the multi-stability of the polygonal origami hypar is still not studied in detail. Therefore, in this paper, we will present a thorough investigation of the multi-stable behavior of the hexagonal origami hypar.

The identification of all stable states is essential for investigating the multi-stability of the hexagonal origami hypar, as it has been experimentally observed to possess more than two stable states. Since the tangent stiffness matrix may become ill-conditioned, simulating the global properties of the hexagonal origami hypar by the same method as used for solving the problem of bistability may be infeasible. Therefore, the simulation of the global behavior needs to be simplified as the kinematic bifurcation analysis of deployable structures [61]. Bifurcations can be determined by the singular value decomposition [62]. A wide range of numerical algorithms has been applied to the geometric, kinematic, or mechanical analysis of origami structures, including the geometric-graph-theoretic method [63], particle swarm optimization method [64], and mixed-integer linear programming method [65]. Another part of studies has simplified multi-stability analysis of systems by bifurcation branches, such as assuming the bifurcation parameters [66,67] and the group- theoretic approach [68,69]. The latter is particularly effective in solving bifurcation branches. More specifically, for structures with highorders of symmetry, it can be simplified according to group theory [70,71]. Based on these theories, Chen et al. [72,73] developed a group-theoretic approach to studying the kinematic behavior of deployable bar structures with cyclic symmetry. However, the applications of group theory and symmetry in the field of origami structures have been largely focused on designing innovative crease patterns (see, e.g. [74–76]), whereas there has been little attention to their folding kinematics and stability problems.

Here, using group theory and its methematical representation capabilities, we propose a new strategy to study the multi-stability of the hexagonal origami hypar. The group-theoretic approach is introduced to simplify the whole folding process of origami structures. The bifurcation branches of origami structures with high orders of symmetry as the hexagonal origami hypar can be solved by symmetry breaking. The corresponding stable states can be obtained by kinematic analysis with the bar-and-hinge models of different bifurcation branches. The bifurcation branches and the corresponding stable states will manifest multi-stability during the entiredeployment process. Moreover, our work will study the effect of material properties on the multi-stability of this structure. This article is organized as following: Section 2 introduces the group-theoretic method for multi-stability analysis; Section 3 demonstrates the multi-stability of the hexagonal origami hypar in different bifurcation branches; Section 4 discusses possible stable states and the effect of crease parameters; finally, Section 5 provides the main concluding remarks of this research.

2. Methodology

We utilize the equivalent bar-and-hinge model to analyze the deformation of the hexagonal origami hypar. Using group theory, the analysis process is simplified to studying bifurcation branches whichcan be obtained by symmetry breaking.

2.1. Bar-and-hinge model of non-rigid origami

The bar-and-hinge model is a simplified model in the finite element analysis of origami [77,78]. On this basis, the total potential energy Π can be expressed as

$$\Pi = U - V \tag{1}$$

where V is the external work and U is the strain energy. According to the principle of the minimum total potential energy, the finite element equation can be expressed as

$$\mathbf{F} = \mathbf{K}\Delta \tag{2}$$

where $\mathbf{F}$, $\mathbf{K}$, and $\mathbf{\Delta}$ donate the force vector, tangent stiffness matrix, andgeneralized displacement vector, respectively. The internal force vector and the tangent stiffness matrix can be assembled from equivalent nodal loads and elementary stiffness matrices.

In comparison with rigid origami, the potential energy U of non-rigid origami contains not only folding energy, but also facet deformation energy [50].

$$U = U_F + U_S + U_B \tag{3}$$

where U_F, U_S, and U_B represent the crease folding energy, bar stretching energy, and facet bending or twisting energy, respectively. Then, the tangent stiffness matrix can be calculated by finding displacement variations of Eq. (3) twice [50].

$$\mathbf{K} = \mathbf{K}_F + \mathbf{K}_S + \mathbf{K}_B = \mathbf{K}_{spr} + \mathbf{K}_{bar} \tag{4}$$

where the stiffness of rotational spring elements $\mathbf{K}_{spr}$ only affects the folding stiffness of the crease $\mathbf{K}_F$. The stiffness of bar elements $\mathbf{K}_{bar}$ contains in-plane stretching and shearing stiffness of the bar $\mathbf{K}_S$ and the out-plane bending stiffness of the facet $\mathbf{K}_B$. Thus, the elementary stiffness of bar elements and rotational spring elements should be calculated. The hyperplastic model is selected to simulate the constitutive relationship of bar elements [77,78]. The elementary stiffness matrices are obtained by

$$\begin{cases} \mathbf{K}^{\mathbf{e}}_{\mathbf{spr}} &= \mathbf{K}^{\mathbf{e}}_{\mathbf{F}} = \partial^2 U^e_F \big/ \partial \mathbf{u}^2 = k^e_{spr} d\theta \big/ d\mathbf{u} \otimes d\theta \big/ d\mathbf{u} + M_F d^2\theta \big/ d\mathbf{u}^2 \\ \mathbf{K}^{\mathbf{e}}_{\mathbf{B}} &= \partial^2 U^e_B \big/ \partial \mathbf{u}^2 = k^e_B d\theta \big/ d\mathbf{u} \otimes d\theta \big/ d\mathbf{u} + M_B d^2\theta \big/ d\mathbf{u}^2 \\ \mathbf{K}^{\mathbf{e}}_{\mathbf{S}} &= \partial^2 U^e_S \big/ \partial \mathbf{u}^2 = k^e_S \left(\mathbf{B}_1^T + \mathbf{B}_2\mathbf{u}\right)\left(\mathbf{B}_1^T + \mathbf{B}_2\mathbf{u}\right)^T + f_s\mathbf{B}_2 \end{cases} \tag{5}$$

During the simulation of the kinematic path, the tangent stiffness matrix near the bifurcations will be severely ill-conditioned. However, it can be effectively avoided by utilizing group theory [79,80].

2.2. A group-theoretic approach to the global bifurcation analysis

Central to performing the global bifurcation analysis is to solve the vector equilibrium equation

$$\mathbf{f}(\mathbf{u},\lambda)=\mathbf{0} \tag{6}$$

where $\mathbf{u}$ belongs to an N-dimensional real vector space and λ is a real number. Then, using the symmetry-adapted coordinate system, the Newton-Rapson procedure can be implemented by the block diagonalization method as follows

$$\begin{bmatrix} \mathbf{K}_{\nu^{(1)}} & 0 & \cdots & 0 \\ 0 & \mathbf{K}_{\nu^{(2)}} & \cdots & 0 \\ \vdots & \vdots & \cdots & \vdots \\ 0 & 0 & \cdots & \mathbf{K}_{\nu^{(p)}} \end{bmatrix} \begin{bmatrix} \Delta\mathbf{u}^{(1)} \\ \Delta\mathbf{u}^{(2)} \\ \vdots \\ \Delta\mathbf{u}^{(p)} \end{bmatrix} = \begin{bmatrix} -\mathbf{f}_{\lambda} \\ 0 \\ \vdots \\ 0 \end{bmatrix} \tag{7}$$

where $\mathbf{K}$ represents the tangent stiffness matrix $\mathbf{K}=\mathrm{d}\mathbf{f}/\mathrm{d}\mathbf{u}$. Decomposed by many block matrices, the original problem can be reduced to a series of independent problems with specific symmetry subspaces.

$$\mathbf{K}_{\nu^{(1)}}\Delta\mathbf{u}^{(1)}=-\mathbf{f}_{\lambda} \tag{8}$$

In other words, the solution of Eq. (6) can be obtained by solving Eq. (8) associated with different subspaces. In particular, for a symmetric structure, the symmetry subgroups are associated with different symmetry subspaces. Therefore, the bifurcation branches of the original structure will consist of the bifurcation branches of the corresponding symmetry subgroups [81].

2.3. Symmetry breaking behavior

The transformation from the primary path to bifurcation paths of deployable structures is often accompanied by symmetry breaking behavior [72,73]. In other words, different bifurcation paths can be obtained by reducing the symmetry order of structures.

The C_{nv} symmetry group contains a total of $2n$ independent symmetry operations [82], and is represented as

$$C_{nv}=\left\{C_n^j,\sigma_j|j=1,2,\cdots,n\right\} \tag{9}$$

where rotation C_n^j represents the rotation of the original structure by an angle $2\pi j/n$ around the symmetry axis, $j\in[1,n]$, and σ_j denotes the j-th reflection along the vertical symmetry plane. Among these symmetry operations, the one-dimensional and two-dimensional irreducible representations are selected to describe the partial symmetry of the original structure. The irreducible representations are expressed as

$$n=\text{even}\begin{cases}\Gamma^{(1)}=A_1,\ \Gamma^{(2)}=A_2,\ \Gamma^{(3)}=B_1,\ \Gamma^{(4)}=B_2 & \text{One}-\text{dimensional}\\ \Gamma^{(5)}=E_1,\ \cdots,\ \Gamma^{(3+0.5n)}=E_{0.5n-1} & \text{Two}-\text{dimensional}\end{cases} \tag{10}$$

$$n=\text{odd}\begin{cases}\Gamma^{(1)}=A_1,\ \Gamma^{(2)}=A_2 & \text{One}-\text{dimensional}\\ \Gamma^{(3)}=E_1,\ \cdots,\ \Gamma^{(1.5+0.5n)}=E_{0.5n-0.5} & \text{Two}-\text{dimensional}\end{cases} \tag{11}$$

where $\Gamma^{(i)}$ denotes an irreducible representation of the structure, and A_1,⋯, B_1,⋯, E_1,⋯ represent the basic symmetry representations. The number of one-dimensional irreducible representations of C_{nv} is $2\alpha+2$, whereas that of two-dimensional irreducible representations is $(n-1-\alpha)/2$ [83]. The value of α equals 0 (or 1) when n is odd (or even). The first and last items indicate the highest and lowestorders of symmetry respectively.. Then, the subgroups can be obtained from these irreducible representations.

$$C_1,\cdots,C_i,\cdots,C_m,C_n,C_v,\cdots,C_{iv},\cdots,C_{mv}\subset C_{nv} \tag{12}$$

where m represents the maximum proper divisor of n, and i includes all the proper divisors of n. Accordingly, the affiliation and symmetry order of these subgroups of C_{nv} can be determined. For instance, C_1 is the lowest-order symmetry group.

A kinematically indeterminate structure is mobile if the symmetry order of the internal mechanism mode is higher than that of the self-stress state [71]. In other words, the symmetry order of the self-stress state has to be reduced to ensure foldability. If the symmetry order of the mechanism mode fails to satisfy the full symmetry, the structure will transform into a bifurcation branch with lower-order symmetry. The bifurcation branch matches the symmetry order of the associated constraint modes. That is, we can effectively program the symmetry order of the structure by controlling the constraint mode.

3. Multi-stability of the hexagonal origami hypar

Fig. 1 shows the crease pattern of a typical hexagonal origami hypar. The blue dashed lines and red solid lines represent the valley and mountain creases, respectively, while the black solid dots represent the z-direction constraints. The geometric and material parameters of the initial pattern are defined according to the square origami hypar in [51]. The fold spacing d and inner fold spacing D are $d=D=8$ mm. The number of the crease layers is $n=8$, the thickness t is 127μm, the elastic modulus E for the material is 5 GPa, and the Poisson's ratio is 0.35. In contrast to the square origami hypar, there are more possibilities for the 3D geometry of the hexagonal origami hypar. In this section, we will investigate the multi-stability of the hexagonal origami hypar by studying its stable states with different symmetry orders.

The initial planar pattern of the hexagonal origami hypar belongs to symmetry group C_{6v}. To allow the structure to be foldable, the symmetry order of the self-stress state is required to be decreased to a value less than that of the initial pattern [71,72]. The subgroups of C_{6v} group can be computed by

$$C_1,C_2,C_3,C_4,C_5,C_6,C_v,C_{2v},C_{3v}\subset C_{6v} \tag{13}$$

According to established theorems for assigning mountain and valley creases [84], crease assignments in the initial patterns must be symmetric with respect to the diagonals. In other words, the initial pattern cannot belong to a symmetry subgroup containing only cyclic rotations, i.e. C_6, C_3, C_2, and C_1. Therefore, we only need to study the cases with mirror symmetries, namely C_{3v}, C_{2v}, and C_v.

According to Section 2, a specific symmetry-breaking of the structure is achieved by adjusting the symmetry order of the constraint mode. Fig. 1(a) shows the three-dimensional view of the pattern, and Figs. 1(b), (c), and (d) depict different constraint modes leading to origami configurations with different symmetry groups. The mountain and valley assignments of the innermost creases depend on the symmetry group. Figs. 1(b), (c), and (d) corresponds to the C_{3v}, C_{2v}, and C_v symmetries, respectively.

3.1. Hexagonal origami hypar with C_{3v} symmetry

Among the subgroups, the highest=symmetry mechanism mode is the C_{3v} symmetry. The initial 3D configuration can be obtained by

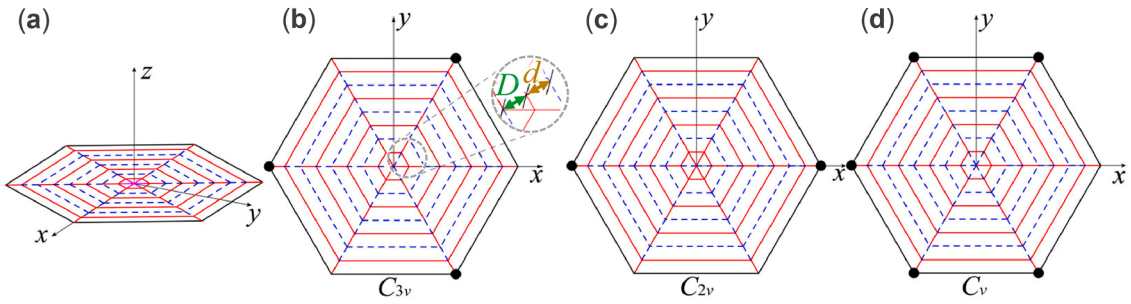

Fig. 1. Crease patterns of the hexagonal origami hypar: (a) Three-dimensional view of the crease pattern. (b- d) Different constraint modes and crease patterns corresponding to symmetry groups C_{3v}, C_{2v}, and C_v.

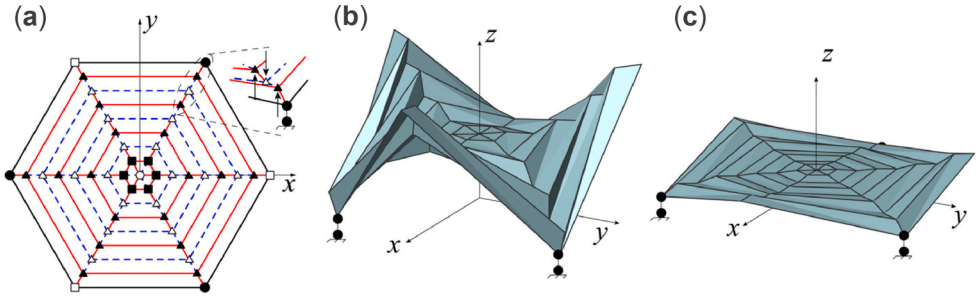

Fig. 2. 3D origami configuration with C_{3v} symmetry. (a) Applied forces in the z-direction (the hollow circle ○ represents downward force F_0, the solid square ■ represents upward force $2.25F_0$, the hollow triangle △ represents downward force $4F_0$, the solid triangle ▲ represents upward force $4F_0$, the hollow square □ represents upward force $2F_0$, and the solid circle ● represents constraints in the z-direction) (b) Initial 3D configuration. (c) 3D configuration in a stable state.

loading the equivalent bar-and-hinge model in the z-direction. The applied forces to fold the initial pattern are adjusted based on the folding of the square origami hypar [51]. The loading in the z-direction used in this study is shown in Fig. 2(a), which provides us with the initial 3D configuration (see Fig. 2(b), obtained using MERLN2_v1.1 based on the constraints and forces depicted in Fig. 2(a)). However, it is a random state rather than a stable state. When the external loads are relieved, the system will recover into one of its stable states, as shown in Fig. 2(c).

In order to find other stable states with C_{3v} symmetry, we further analyze the stable 3D configurations by using the bar-and-hinge model. In Fig. 3(a1), the three lower outermost vertices are constrained, whereas downward displacements are applied to the remaining three vertices. As displacements increase, the structure first unfolds from the first stable state (State 1) to an approximately fully flat state (State 2). Then, it refolds along the creases to a new equilibrium (State 3). Importantly, the total potential energy reaches another minimum at State 3, as shown in Fig. 3(e). According to the energy principle, the new equilibrium is the second stable state of the hexagonal origami hypar with C_{3v} symmetry.

The stored energy-displacement relation clearly manifests the bistability of the structure. In Fig. 3(e), the total potential energy E_T contains the tensile and shear energy E_S, the bending energy E_B, and the folding energy E_F. During the transition from the stable State 1 to the stable State 3, E_F increases with the decrease of the folding angle and accounts for the largest proportion of E_T. This property indicates that this structure folds preferentially at the creases. The facet deformation energy $E_B + E_S$ accounts for a certain proportion of the total potential energy, especially when the structure is close to the stable states. Thus, in terms of the folding energy, the facet deformation energy cannot be ignored. In other words, the hexagonal origami hypar is a non-rigid origami structure the facet deformations of which need to be considered during the folding process.

Concerning the specific composition of the deformation energy, E_S increases while E_B decreases with the flattening of the facets. E_B accounts for the most of the facet deformation energy around the stable states whereas E_S accounts for the most of the facet deformation energy near the fully-expanded state. That is, the deformation of the facets is dominated by bending near the stable states, and by tension, compression, and shear near the fully-expanded state. Moreover, E_B changes substantially during the entire process while E_S only changes considerably near the fully flattened state. This implies that the bending deformation of the facets exists in the entire process while the tensile deformation of the facets only occurs near the fully flattened state. In addition, the proportion of E_S in E_T is still small even near the fully expanded state, whereas the proportion of E_B in E_T is large near the stable states. Therefore, it can be concluded that the facets deformation of the hexagonal origami hypar is mainly controlled by the bending deformation.

The equilibrium load-displacement curves further verify these two stable states. In Fig. 3(d), these two stable states correspond exactly to the two zero points that cross the reference line $F = 0$ in the positive direction. State P1 and State P2 both reach the peak value of the equilibrium load during folding and unfolding. Moreover, according to Fig. 3 (d), they are roughly symmetric about the center point corresponding to State 2. Similarly, the two stable states (i.e., State 1 and State 3) are symmetric about State 2 as the center point. Fig. 3(c) shows the changing profile of the $y = 0$ section during folding. The two stable states (i.e., State 1 and State 3) and the two peak force states (i.e., State P1 and State P2) are mirror symmetric along $x = 0$. The intermediate State 2 is mirror symmetric about the x-axis, but not fully flattened. Moreover, except for the innermost folds, the mountain and valley properties of the creases remain constant during the transition between the two stable states.

3.2. *Hexagonal origami hypar with C_{2v} symmetry*

The first stable state with C_{2v} symmetry is obtained by the same method described at the beginning of Section 3.1. The main difference is that this case requires the origami pattern and constraints shown in Fig. 1(c). The unconstrained outermost vertices are all load points in this

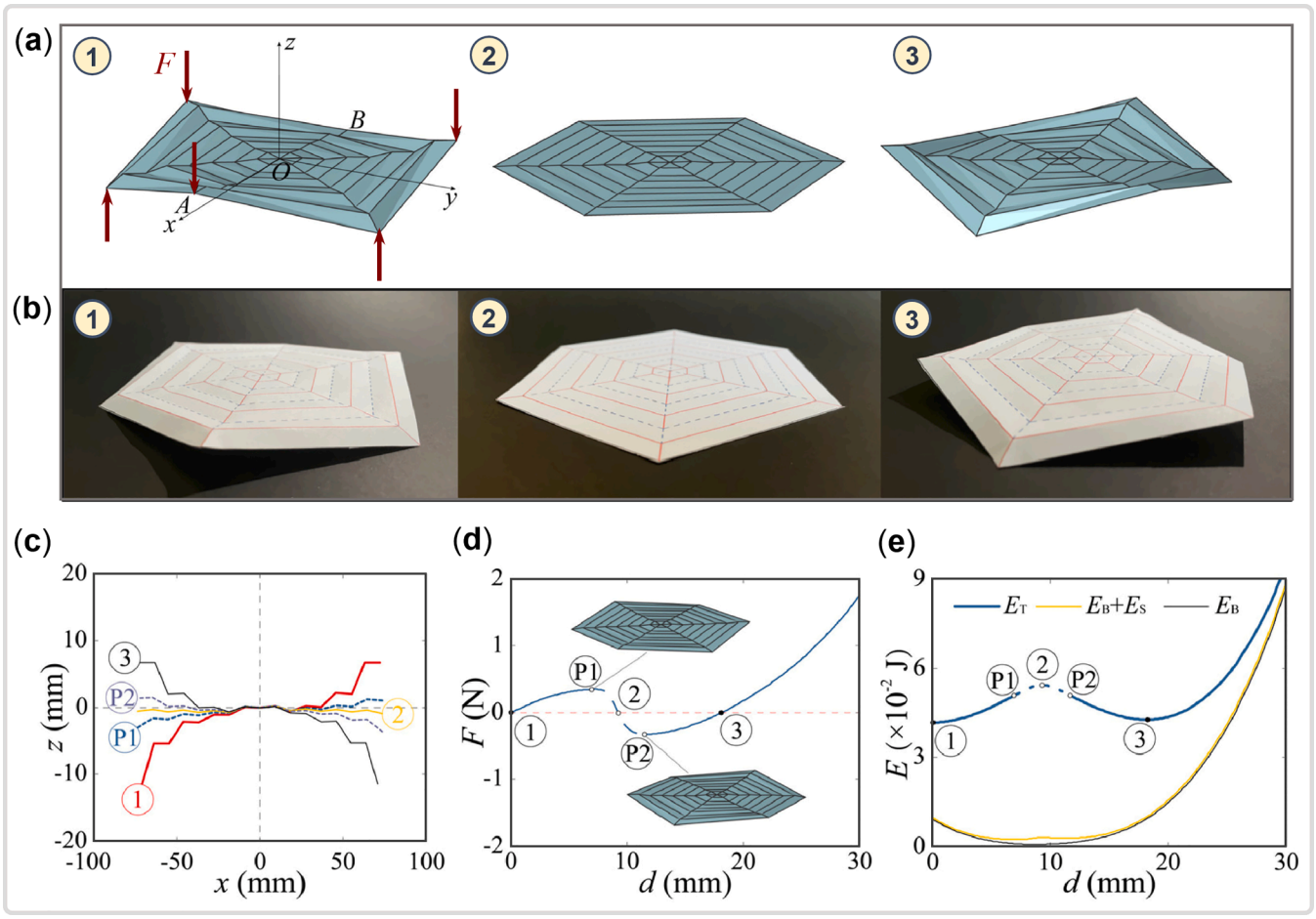

Fig. 3. Multi-stability of the hexagonal origami hypar with C_{3v} symmetry. (a) Three key states of the shape transition process. (b) A physical models in the three key states. (c) Changing profile of the set of diagonal creases on the *x*-axis (i.e., diagonal *AOB*). (d) Equilibrium load versus displacement curves of single load point. (e) Stored energy versus displacement curves.

case because the constraint conditions have been altered. The load size and direction of the new load points are the same as the load size and direction represented by the hollow square □ in Fig. 2(a). The loading conditions for the remaining nodes are the same as those shown in Fig. 2 (a).

Here, we analyze the stable 3D configurations with C_{2v} symmetry by a similar method as in Section 3.1. The two outermost vertices on an adjacent diagonal are constrained, and upward loads are applied to the remaining four outermost vertices on two adjacent diagonals. Then, two lower outermost vertices are constrained, whereas the downward displacements are applied to the remaining four outermost vertices, as shown in Fig. 4(a1). As displacements increase, the structure first unfolds from the initial stable State 1 to approximately fully flattened State 2. Then, it refolds along the creases to a new equilibrium State 3. The total potential energy at State 3 reaches another minimum, as shown in Fig. 4(e). According to the energy principle, the new equilibrium is the second stable state of the hexagonal origami hypar with C_{2v} symmetry.

Similar to the hexagonal origami hypar with C_{3v} symmetry, in Fig. 4 (e), the bistability of the hexagonal origami hypar with C_{2v} symmetry can be directly seen from the stored energy versus displacement curves. As can be seen from Fig. 4(e), the hexagonal origami hypar with C_{2v} symmetry is non-rigid, and the deformations of its facets are dominantly controlled by the bending deformation. Moreover, the variation tendencies of equilibrium load and potential energy during the transition between the two stable states illustrated in Fig. 4(d) and 4(e) are similar to those shown in Fig. 3(d) and 3(e), respectively. Fig. 4(c) reflects the same mountain and valley properties of the creases and symmetry between corresponding states during the entire process. In contrast to the hexagonal origami hypar with C_{3v} symmetry, the key states during the entire transition of this structure are all mirror symmetric about $x = 0$.

3.3. *Hexagonal origami hypar with C_v symmetry*

The 3D configuration with C_v symmetry can be achieved by the further reduction of the symmetry order. The first stable state with C_v symmetry is obtained by the same method as explained in Section 3.1. The origami pattern and constraints of this structure are shown in Fig. 1 (c). The only outermost free vertex is subjected to an upward load of $3F_0$ in the *z*-direction. The loading conditions for the remaining nodes are the same as those shown in Fig. 2(a).

For this origami hypar with C_v symmetry, the five outermost vertices are constrained, and upward loads are applied to the remaining outermost vertex. Then, the five lower outermost vertices are constrained and an downward displacement is applied to the remaining vertex, as shown in Fig. 5(a1). As the displacement increases, the structure first unfolds from the first stable State 1 to an approximately fully flattened State 2. Then, it refolds along the creases to a new stable State 3. The total potential energy reaches another minimum at State 3, as shown in Fig. 5 (e). According to the energy principle, the new equilibrium is the second stable state of the hexagonal origami hypar with C_v symmetry.

Similar to the two cases studies earlier in this paper, the bistability of the hexagonal origami hypar with C_v symmetry can be demonstrated by Fig. 5(e). It is a non-rigid origami structure with facet deformations

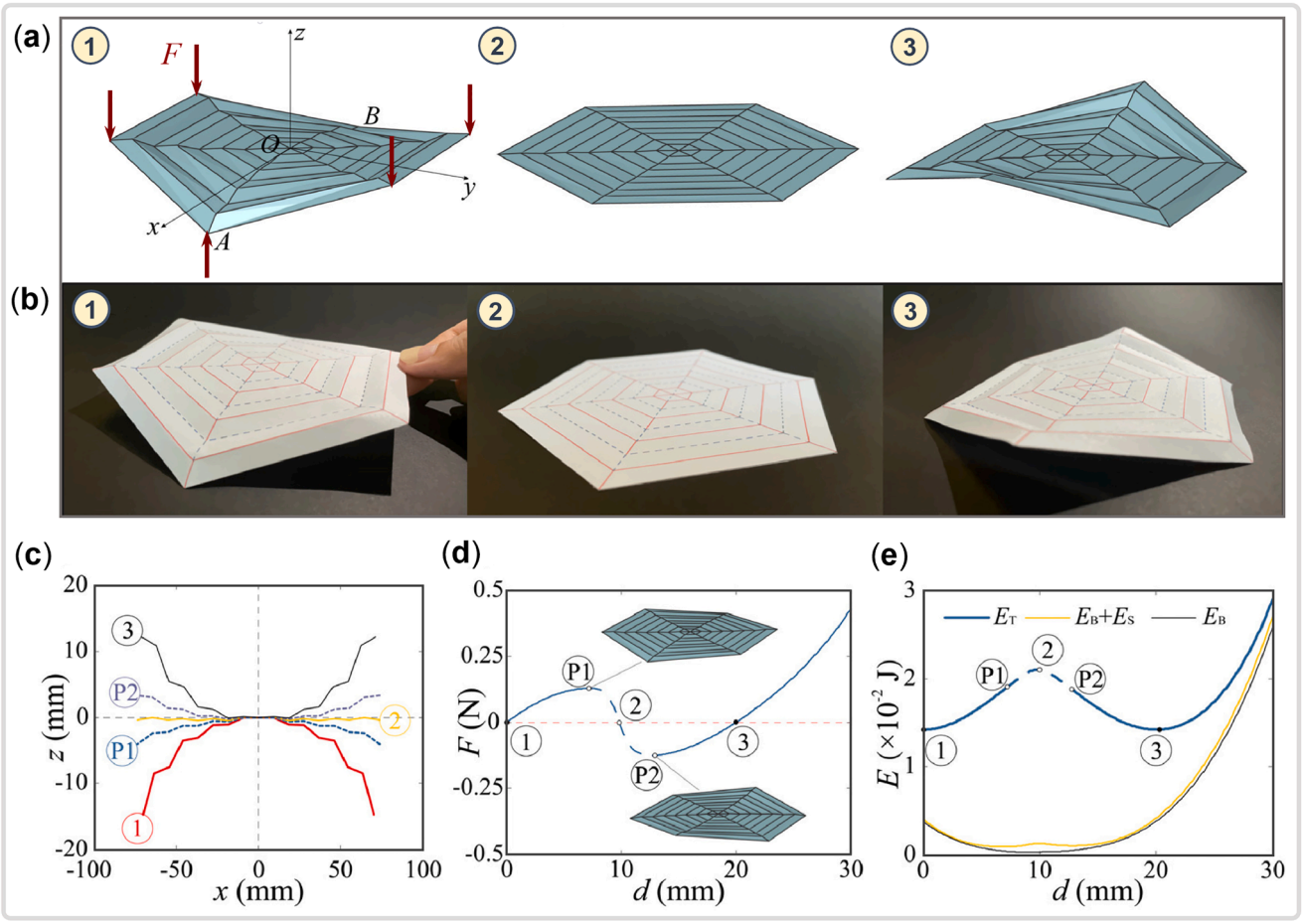

Fig. 4. Multi-stability of the hexagonal origami hypar with C_{2v} symmetry. (a) Three key states of the shape transition process. (b) A physical model in the three key states. (c) Changing profile of the set of diagonal creases on the x-axis (i.e., diagonal AOB). (d) Equilibrium load versus displacement curves of a single load point. (e) Stored energy versus displacement curves.

which are mainly regulated by bending. Moreover, Fig. 5(d) and Fig. 5 (e) indicate similar variation tendencies of the equilibrium load and potential energy as those of the other bifurcation paths. Fig. 5(c) depicts the same mountain and valley properties of the creases during the entire process as in Fig. 3(c) and Fig. 4(c). Compared to the hexagonal origami hypars with C_{3v} and C_{2v} symmetries, the key states of this structure show no symmetry in the $y = 0$ section.

In summary, the bistability of the hexagonal origami hypar in each bifurcation branch is the same as the square origami hypar [43]. There are two stable states along each bifurcation branch. The two stable states in the same bifurcation branch are approximately symmetric along the horizontal plane. Except for the innermost folds, the mountain and valley properties of the creases remain unchanged between these two stable states.

4. Discussion

In this section, we discuss the differences among these three bifurcation branches. Several metrics are chosen to represent the energy barrier of multistable transitions in Section 4.1, and some relevant influencing factors are studied in Section 4.2.

4.1. Multi-stability of the hexagonal origami hypar with different symmetries

To compare and discuss different bifurcation branches, we transform them into a unified coordinate system, as shown in Fig. 6. Points I_a, $P1_a$, $P2_a$, III_a, points I_b, $P1_b$, $P2_b$, III_b, and points I_c, $P1_c$, $P2_c$, III_c correspond to the key States 1, P1, P2, and 3 on the bifurcation branches with C_v, C_{2v} and C_{3v} symmetries described in Section 3, respectively. To ensure the fairness of the comparison among the different numbers of loading points for different bifurcation branches, the total equilibrium load is chosen as the y-axis. In Section 3, we obtained the equilibrium load curves at a single loading point for each bifurcation branch. Therefore, the total equilibrium load should be the sum of the equilibrium loads at all loading points in each branch. Then, based on the symmetry of each bifurcation branch, the equilibrium loads of all the loading points will be identical. That is, we can obtain the total equilibrium load by multiplying the equilibrium load at a single load point by the number of loading points. For the bifurcation branch with C_{3v} symmetry, we applied downward displacements on the three outmost free vertices. Thus, the total equilibrium load bifurcation branch with C_{3v} symmetry will be equal to the equilibrium load at a single loading point multiplied by three. For the bifurcation branch with C_{2v} symmetry, there are four loading points. Therefore, its total equilibrium load will be equal to the equilibrium load at a single loading point multiplied by four. For the bifurcation branch with C_v symmetry, we only applied downward displacement on one vertex. As a results, the total equilibrium load of the bifurcation branch with C_v symmetry will be equal tothe equilibrium load at a single loading point itself.

According to Fig. 6(a), seven possible critical points can be found in total, including point X, Y, Z, X', Y', Z', and II. Fig. 6(c) shows the profiles of the $y = 0$ section of the structure in each bifurcation branche at State 2. Since the displacements are calculated by finite element

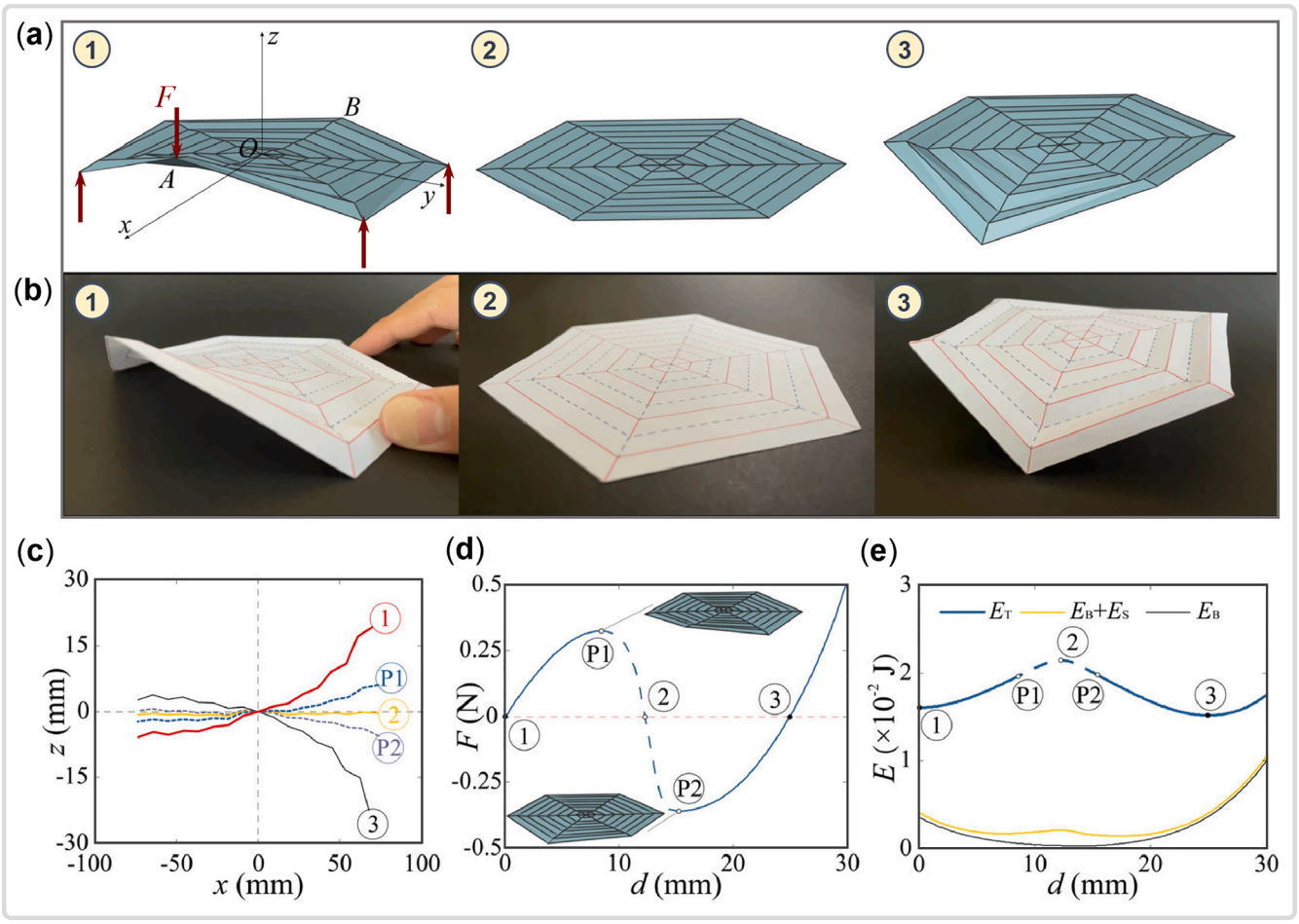

Fig. 5. Multi-stability of the hexagonal origami hypar with C_v symmetry. (a) Three key states of the shape transition process. (b) A physical model in the three key states. (c) Changing profile of the set of diagonal creases on the *x*-axis (i.e., diagonal *AOB*). (d) Equilibrium load versus displacement curves of a single load point. (e) Stored energy versus displacement curves.

analysis, the State 2 shown in Fig. 6(c) is an approximate solution. However, it can be judged from the folding tendency that the hexagonal origami hypar is fully expanded in State 2 as point II in Fig. 6(d). Importantly, point II is one of the critical points of these three bifurcation branches. As for the other possible critical points, the states corresponding to various bifurcation branches at the intersections are different. In Fig. 6(d), these three bifurcation branches have no intersection except point II. In other words, point II is the only critical point of these three bifurcation branches.

We select the state corresponding to the critical point II as the zero potential energy state. Fig. 6(e) shows the total energy (E_T) variation of the hexagonal origami hypar from the stable State 1 to the stable State 3. Critical point II represents the fully flattened state in the three bifurcation branches. The energy barrier of conversion among these stable states can be reflected by the difference between the extreme values of the stored energy curves. In comparison with the stable states with C_{2v} and C_v symmetries, unfolding from the stable state with C_{3v} symmetry to the fully unfolded state is the most difficult transformation to achieve. Unfolding from the stable states with C_{2v} symmetry is relatively easier, while this is the easiest for the stable states with C_v symmetry. In other words, the stable states with C_{3v} symmetry have the greatest energy barrier against transformations to the other stable states, followed by the stable states with C_{2v} symmetry; the stable states with C_v symmetry have the slightest energy barrier.

4.2. *Influence of geometric parameters*

To obtain more general conclusions, here we examine and discuss the effects of different geometric parameters on the stable states of the hexagonal origami hypar, including the thickness of material *t* and the fold spacing *d*. The geometric parameters of different numerical examples are summarized in Table 1.

4.2.1. *Influence of material thickness*

Various geometric parameters associated with each model are listed in Table 1. We utilize the same method, as used for the reference model T0, to simulate the multi-stability of models T1 to T4. Fig. 7(a), (c), and (e) show the results corresponding to C_{3v}, C_{2v}, and C_v symmetries, respectively. Point $T0_I$ represents the stable State 1 in model T0, and the point $T0_{III}$ represents the stable State 3 in model T0.

Fig. 7(a), (c), and (e) show that the peak values of the equilibrium load increase with the material thickness during the transitions of two stable states. The absolute value of *F* indicates its structural height, and the sign (positive or negative) of *F* indicates whether it increases along the positive *z*-axis. If *F* increases along the positive *z*-axis, it is negative; otherwise, *F* is positive. To make the results clearer, we have extracted the peaks of the balanced load and marked them in Fig. 7(b), (d), and (f). The equilibrium load versus height curves during the transition between two stable states consists of two peaks, and the tendencies of them are centrosymmetric along the origin point. The entire process can be divided into two phases with the origin as the cut-off point. The first phase, called the loading phase, is the transition from stable State 1 to a

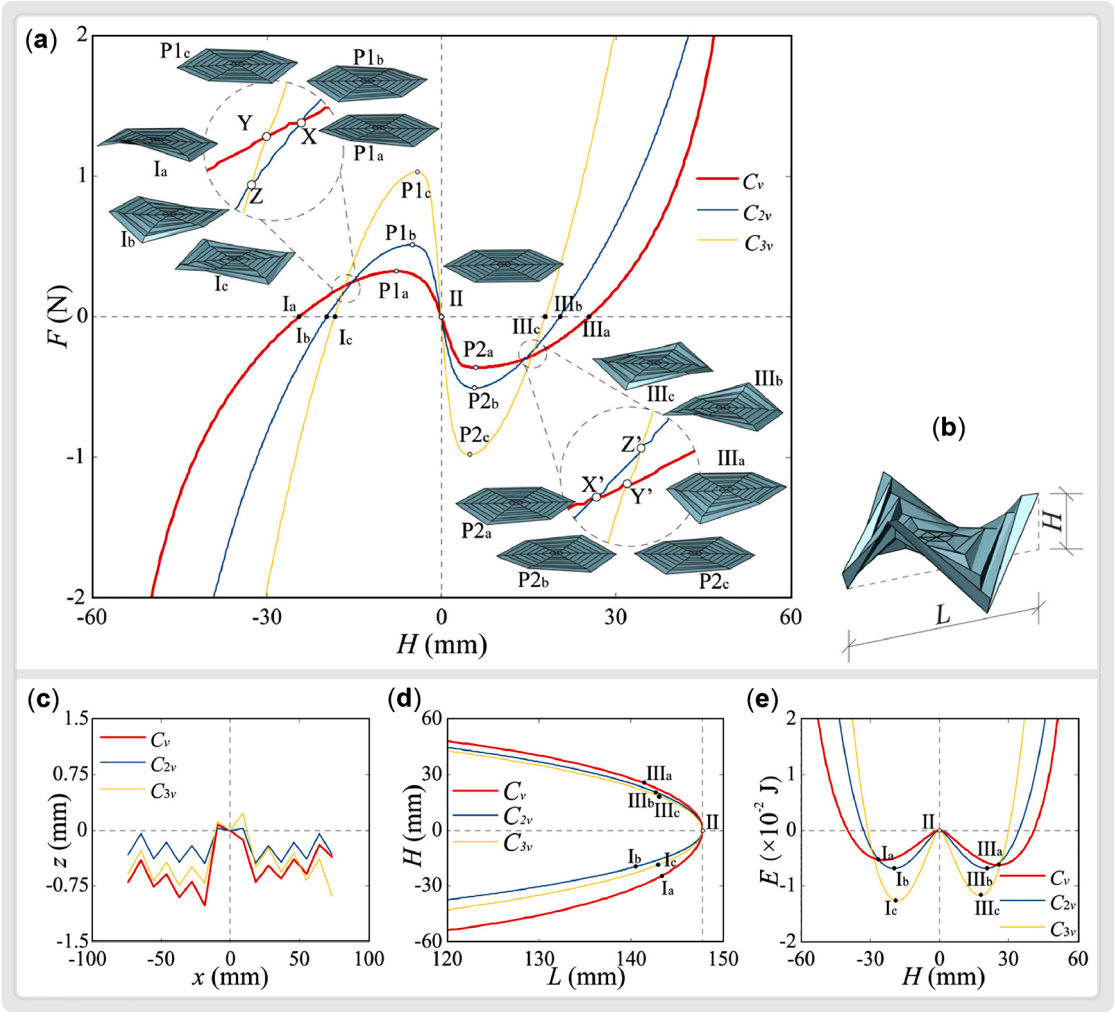

Fig. 6. Comparison among various bifurcation branches. (a) Total equilibrium load-displacement curves of the three bifurcation branches. (b) Physical representation of span (L) and height (H). (c) Profile of the $y = 0$ section in State 2. (d) Span versus height curves. (e) Total energy versus height curves.

Table 1
Geometric parameters of numerical examples.

Model	T0	T1	T2	T3	T4	F1	F2	F3	F4	F5
L (mm)	64	64	64	64	64	60	60	60	60	60
D (mm)	8	8	8	8	8	12	12	12	12	12
d (mm)	8	8	8	8	8	4	6	8	12	16
t (μm)	127	40	76	200	240	127	127	127	127	127

fully flatted state under external loads. Similarly, the second phase, called the recovery phase, is the transition from the fully flatted state to the other stable State 3. The peak equilibrium load in the loading phase is F_L, and the peak equilibrium load in the recovery phase is F_R. Fig. 7(b), (d), (f) show that F_L and F_R are proportional to the third power of the material thickness (i.e., t^3). The fitting plots f_L and f_R in Fig. 7(b), (d), and (f) are obtained by a linear fitting with t^3 as the independent variable in MATLAB.

In the simulation process, the stiffness of the creases and the bending stiffness of the facets are related to t^3, whereas the tension-compression stiffness of the facets is related to t [77]. Similar to the results presented in Section 3, we can conclude that the folding of the structure is mainly realized by the folding of creases and the bending of facets, and the tension and compression deformations of facets only account for a small part.

As for the height of the structure, we refer to the height at which the structure reaches a stable state as the stable height H. Fig. 7(a), (c), and (e) show that the stable height increases with material thickness. Similar to the peak equilibrium load, each equilibrium load-height curve has two stable heights corresponding to the two stable states. The stable height corresponding to stable State 1 is called H_I and the stable height corresponding to stable State 3 is called H_{III}. The absolute value of H is its height and the plus or minus sign indicates whether H increases along the positive z-axis. If H increases along the positive z-axis, it is positive. Otherwise, H is negative. Thus, for the equilibrium load versus height curve, the farther the stable state from $H = 0$, the higher the stable height will be.

In summary, the peak equilibrium loads and the stable heights with the same symmetry, all increase with material thickness. In particular, the magnitude of the peak equilibrium load is positively related to the third power of the material thickness.

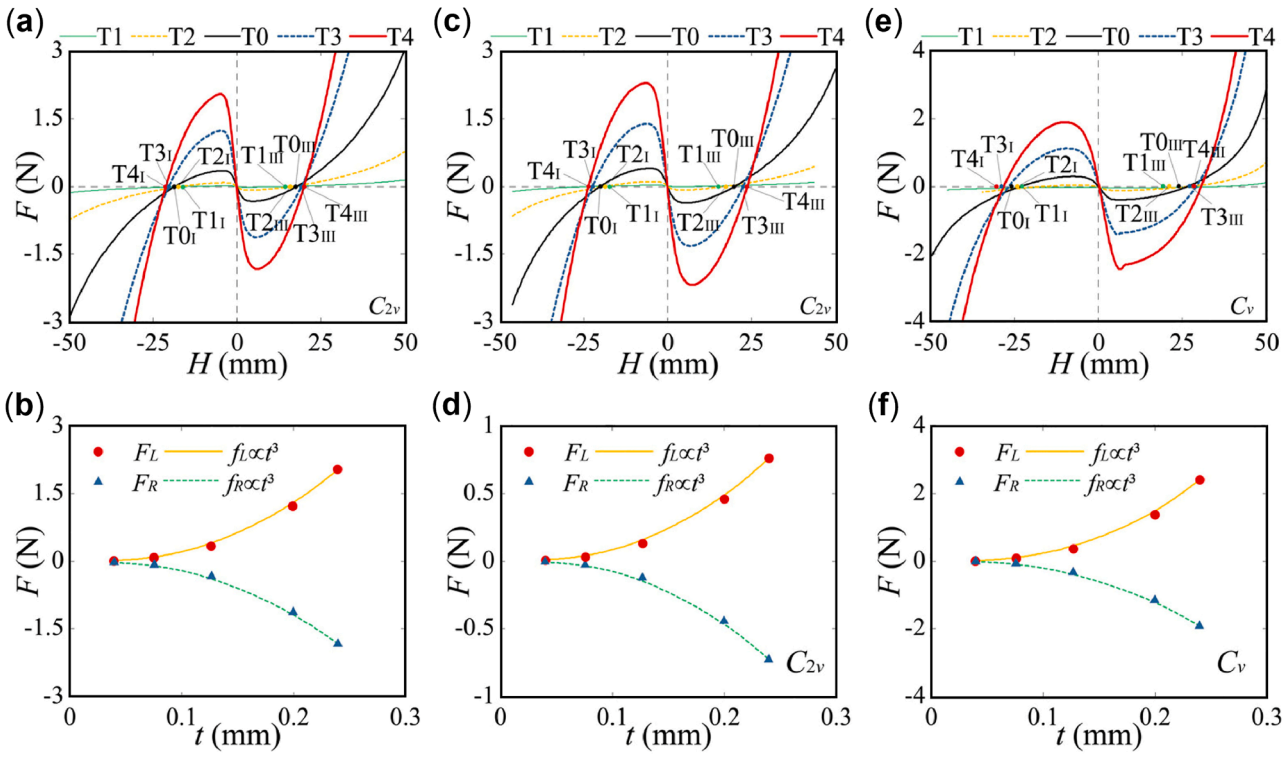

Fig. 7. Effects of material thickness. (a), (c), and (e): Equilibrium load versus height curves of a single load point. (b), (d), and (f): Relationship between the material thickness t and the peak equilibrium load F.

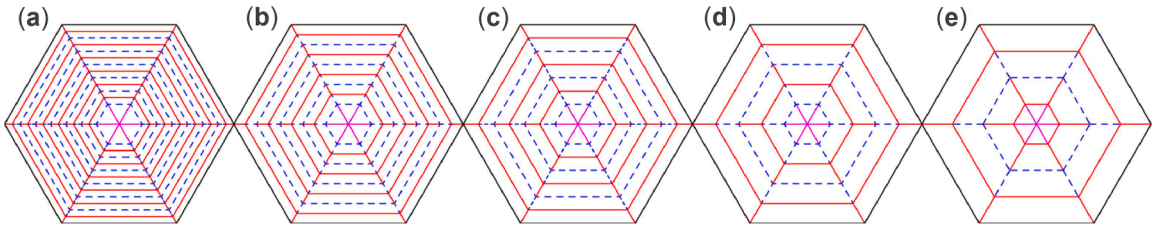

Fig. 8. Crease patterns with different values for parameter d. Sub-figures (a) to (e) correspond to models F1 to F5, respectively.

4.2.2. Influence of crease length

We adjust the geometric parameters of the reference model to the variation of d while keeping L constant. Parameter n varies with d as models F1 to F5 (see Table 1). The outermost creases are kept at peak and various patterns are generated as shown in Fig. 8. Then, the bistability of models F1 to F5 can be simulated. Fig. 9(a) to (c) show the results corresponding to C_{3v}, C_{2v}, and C_v symmetries, respectively. Point $F1_{P1}$ represents State P1 in model F1, and point $F1_{P2}$ represents State P2 in model F1.

In Fig. 9, the peak equilibrium loads increase with creases spacing d during the transitions of two stable states with the same symmetry. Since L does not change, the change of d will directly lead to the change of n. For simplicity, we unify these two variables as the total length of all creases, called crease length (denoted by l). The relationships between the crease length and the peak equilibrium loads are shown in Fig. 9(d). For the three different symmetry cases, the peak equilibrium loads in both the loading and recovery phases increase with crease length. In other words, hexagonal origami hypars with longer crease lengths are more difficult to be folded. As for the stable height, it is related to the crease spacing, crease layers number and crease length. The details of their influence need to be further studied.

In summary, the magnitudes of peak balanced loads increase with increasing the crease length. In other words, the stable states of hexagonal origami hypars with longer crease lengths have more significant energy barriers. The effects of different spans L and the number of initial polygon sides on the stable states of the hexagonal origami hypar can be further studied. The obtained data can be analyzed using deep learning [85] methodsto develop a more precise numerical model, and could facilitate the design of novel programmable metamaterials [86, 87] based on the hexagonal origami hypar.

5. Conclusions

In this work, we utilized a bar-and-hinge model, a group-theoretic approach, and a symmetry breaking process for exploring the multi-stability of the hexagonal origami hypar. The bar-and-hinge model was applied to simulating the entire folding and unfolding process of the structure. Concurrently, the group-theoretic approach was exploited to avoid singularities in the stiffness matrix near the bifurcations. The symmetry subgroups obtained by symmetry breaking were introduced to trace the corresponding bifurcation branches. The multi-stability of the structure was demonstrated by analyzing the multi-stability of all the bifurcation branches. The main conclusions of this study can be summarized as follows:

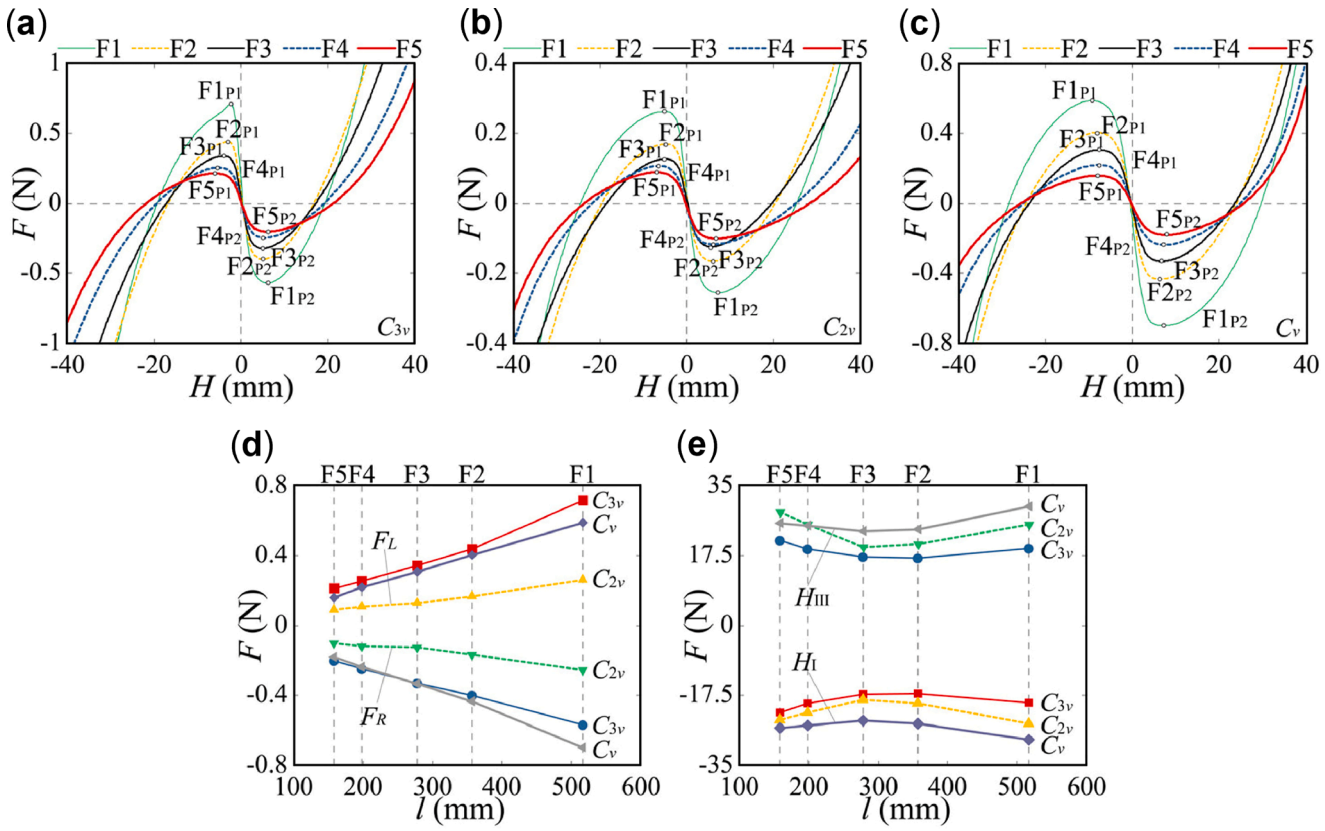

Fig. 9. Effect of crease spacing. (a) to (c) Equilibrium load versus height curves of a single load point. (d) Relationship between the creases length l and the peak equilibrium loads F_L and F_R. (e) Relationship between the creases length l and the stable heights H_I and H_{III}.

1) The hexagonal origami hypar is always non-rigid during folding. Its non-rigid deformation is mainly realized by the bending deformation of each facet.
2) The exagonal origami hypar has three distinct types of bifurcation paths, including C_{3v}, C_{2v}, and C_v symmetries. All the bifurcation branches exhibit bistability. Thus, the hexagonal origami hypar has six independent stable states.
3) These stable states can be converted to each other only through the fully flattened state. The initial state with the greatest energy barrier is the stable states with C_{3v} symmetry, and the slightest one is the stable states with C_v symmetry. The energy barrier increases with increasing the material thickness or the crease length.

Furthermore, the method proposed in this study can be extended for the multi-stability analysis of origami structures with higher-order symmetries. It can systematically describe the transitions among their stable states by converting the original folding analysis into a collection of multi-stability investigations in different bifurcation branches.

CRediT authorship contribution statement

Yao Chen: Methodology, Resources, Formal analysis, Validation, Investigation, Writing – original draft, Writing – review & editing, Supervision, Project administration, Funding acquisition. **Ruizhi Xu:** Conceptualization, Investigation, Data curation, Formal analysis, Validation, Methodology, Software, Writing – original draft. **Chenhao Lu:** Formal analysis, Software, Writing – review & editing. **Ke Liu:** Supervision, Methodology, Validation, Writing – review & editing. **Jian Feng:** Supervision, Validation, Writing – review & editing. **Pooya Sareh:** Supervision, Validation, Writing – review & editing, Funding acquisition.

Declaration of Competing Interest

The authors declare that they have no known competing financial interests or personal relationships that could have appeared to influence the work reported in this paper.

Data availability

Data will be made available on request.

Acknowledgement

This work was supported by the National Natural Science Foundation of China (Grants No. 51978150 and 52050410334), Southeast University "Zhongying Young Scholars" project, and the Fundamental Research Funds for the Central Universities. KL acknowledges the support by Peking University, College of Engineering. The authors are grateful to the editors and anonymous reviewers for their professional comments and valuable suggestions in improving the quality of the paper.

References

[1] Siefert E, Reyssat E, Bico J, Roman B. Bio-inspired pneumatic shape-morphing elastomers. Nat Mater 2019;18(1):24–8. https://doi.org/10.1038/s41563-018-0219-x.
[2] Huang C, Tan T, Hu X, Yang F, Yan Z. Bio-inspired programmable multi-stable origami. Appl Phys Lett 2022;121(5):51902. https://doi.org/10.1063/5.0088242.
[3] Li Z, Yang Q, Fang R, Chen W, Hao H. Origami metamaterial with two-stage programmable compressive strength under quasi-static loading. Int J Mech Sci 2021;189:105987. https://doi.org/10.1016/j.ijmecsci.2020.105987.
[4] Meng Z, Chen W, Mei T, Lai Y, Li Y, Chen CQ. Bistability-based foldable origami mechanical logic gates. Extreme Mech Lett 2021;43:101180. https://doi.org/10.1016/j.eml.2021.101180.

[5] Yi S, Wang L, Chen Z, Wang J, Song X, Liu P, Zhang Y, Luo Q, Peng L, Wu Z, Guo CF, Jiang L. High-throughput fabrication of soft magneto-origami machines. Nat Commun 2022;13(1). https://doi.org/10.1038/s41467-022-31900-5.
[6] Kaufmann J, Bhovad P, Li S. Harnessing the multistability of kresling origami for reconfigurable articulation in soft robotic arms. Soft Robot 2022;9(2):212–23. https://doi.org/10.1089/soro.2020.0075.
[7] Sareh P, Chermprayong P, Emmanuelli M, Nadeem H, Kovac M. The spinning cyclic 'Miura-oRing'for mechanical collision-resilience. Origami 2018;7(3): 981–94.
[8] Sareh P, Chermprayong P, Emmanuelli M, Nadeem H, Kovac M. Rotorigami: A rotary origami protective system for robotic rotorcraft. Sci Robot 2018;3(22): eaah5228.
[9] Mirkhalaf M, Barthelat F. Design, 3D printing and testing of architectured materials with bistable interlocks. Extreme Mech Lett 2017;11:1–7. https://doi.org/10.1016/j.eml.2016.11.005.
[10] Qiu H, Feng Y, Gao Y, Zeng S, Tan J. The origami inspired design of polyhedral cells of truss core panel. Thin-Walled Struct 2021;163:107725. https://doi.org/10.1016/j.tws.2021.107725.
[11] Mehreganian N, Fallah AS, Sareh P. Structural mechanics of negative stiffness honeycomb metamaterials. J. Appl. Mech. 2021;88(5).
[12] Zhang Y, Wang Q, Tichem M, van Keulen F. Design and characterization of multi-stable mechanical metastructures with level and tilted stable configurations. Extreme Mech Lett 2020;34:100593. https://doi.org/10.1016/j.eml.2019.100593.
[13] Yasuda H, Tachi T, Lee M, Yang J. Origami-based tunable truss structures for non-volatile mechanical memory operation. Nat Commun 2017;8(1):962. https://doi.org/10.1038/s41467-017-00670-w.
[14] Bhovad P, Kaufmann J, Li S. Peristaltic locomotion without digital controllers: exploiting multi-stability in origami to coordinate robotic motion. Extreme Mech Lett 2019;32:100552. https://doi.org/10.1016/j.eml.2019.100552.
[15] Novelino LS, Ze Q, Wu S, Paulino GH, Zhao R. Untethered control of functional origami microrobots with distributed actuation. Proc Natl Acad Sci 2020;117(39): 24096–101. https://doi.org/10.1073/pnas.2013292117.
[16] Zhai Z, Wang Y, Jiang H. Origami-inspired, on-demand deployable and collapsible mechanical metamaterials with tunable stiffness. Proc Natl Acad Sci-PNAS 2018; 115(9):2032–7. https://doi.org/10.1073/pnas.1720171115. 1.
[17] Zhang X, Ma J, Li M, You Z, Wang X, Luo Y, Ma K, Chen Y. Kirigami-based metastructures with programmable multistability. Proc Natl Acad Sci 2022;119 (11). https://doi.org/10.1073/pnas.2117649119.
[18] Fang H, Wang KW, Li S. Asymmetric energy barrier and mechanical diode effect from folding multi-stable stacked-origami. Extreme Mech Lett 2017;17:7–15. https://doi.org/10.1016/j.eml.2017.09.008.
[19] Li S, Wang KW. Fluidic origami with embedded pressure dependent multi-stability: a plant inspired innovation. J. R Soc Interface 2015;12(111):20150639. https://doi.org/10.1098/rsif.2015.0639.
[20] Miura K. Map Fold a La Miura Style, Its Physical Characteristics and Application to the Space Science. Takaki (Ed.), Research of pattern formation, KTK Scientific Publishers (1994), pp. 77-90.
[21] Sareh P. Symmetric Descendants of the Miura-ori. PhD Dissertation, Engineering Department, University of Cambridge, UK (2014).
[22] Ginepro J, Hull TC. Counting Miura-ori Foldings. J Integer Seq 2014;17(10):14-10.
[23] Stachel H. Remarks on miura-ori, a japanese folding method. In: *International Conference on Engineering Graphics and Design*. 12. Romania: Technical University of Cluj-Napoca; 2009.
[24] Miura K. Map, Origami, and Space: A Study on Miura-ori. *Journal of the Japan Cartographers Association* 35.2 (1997): 1-10.
[25] Sareh P, Guest SD. Design of isomorphic symmetric descendants of the Miura-ori. Smart Mater Struct 2015;24(8):085001.
[26] Sareh P, Guest SD. Design of non-isomorphic symmetric descendants of the Miura-ori. Smart Mater Struct 2015;24(8):085002.
[27] Sareh P, Guest SD. Designing symmetric derivatives of the Miura-ori. In: *Advances in Architectural Geometry 2014*. Springer International Publishing; 2015. p. 233–41.
[28] Lv Y, Zhang Y, Gong N, Li ZX, Lu G, Xiang X. On the out-of-plane compression of a Miura-ori patterned sheet. Int. J. Mech. Sci 2019;161:105022.
[29] Miura M, Hull T. The application of origami science to map and atlas design. Origami 2002;3:137–46.
[30] Hull TC. *Origametry: Mathematical methods in paper folding*. Cambridge University Press; 2020.
[31] Hull Thomas. *Project origami: activities for exploring mathematics*. CRC Press; 2012.
[32] Yasuda H, Yang J. Reentrant origami-based metamaterials with negative Poisson's ratio and bistability. Phys Rev Lett 2015;114(18):185502. https://doi.org/10.1103/PhysRevLett.114.185502.
[33] Yamaguchi K, Yasuda H, Tsujikawa K, Kunimine T, Yang J. Graph-theoretic estimation of reconfigurability in origami-based metamaterials. Mater Des 2022; 213:110343. https://doi.org/10.1016/j.matdes.2021.110343.
[34] Fang H, Zhang Y, Wang KW. Origami-based earthworm-like locomotion robots. Bioinspir Biomim 2017;12(6):65003. https://doi.org/10.1088/1748-3190/aa8448.
[35] Han H, Tang L, Cao D, Liu L. Modeling and analysis of dynamic characteristics of multi-stable waterbomb origami base. Nonlinear Dyn 2020;102(4):2339–62. https://doi.org/10.1007/s11071-020-06082-8.
[36] Lu L, Dang X, Feng F, Lv P, Duan H. Conical kresling origami and its applications to curvature and energy programming. Proc R Soc A-Math Phys Eng Sci 2022;478 (2257):20210712. https://doi.org/10.1098/rspa.2021.0712.
[37] Tao R, Ji L, Li Y, Wan Z, Hu W, Wu W, Liao B, Ma L, Fang D. 4D printed origami metamaterials with tunable compression twist behavior and stress-strain curves. Compos Part B 2020;201:108344. https://doi.org/10.1016/j.compositesb.2020.108344.
[38] Silverberg JL, Na J, Evans AA, Liu B, Hull TC, Santangelo CD, Lang RJ, Hayward RC, Cohen I. Origami structures with a critical transition to bistability arising from hidden degrees of freedom. Nat Mater 2015;14(4):389–93. https://doi.org/10.1038/nmat4232.
[39] Ma J, Zang S, Feng H, Chen Y, You Z. Theoretical characterization of a non-rigid-foldable square-twist origami for property programmability. Int J Mech Sci 2021; 189:105981. https://doi.org/10.1016/j.ijmecsci.2020.105981.
[40] Yasuda H, Johnson K, Arroyos V, Yamaguchi K, Raney JR, Yang J. Leaf-like origami with bistability for self-adaptive grasping motions. Soft Robotics 2022. https://doi.org/10.1089/soro.2021.0008.
[41] Kamrava S, Mousanezhad D, Ebrahimi H, Ghosh R, Vaziri A. Origami-based cellular metamaterial with auxetic, bistable, and self-locking properties. Sci Rep 2017;7(1). https://doi.org/10.1038/srep46046.
[42] Kamrava S, Ghosh R, Wang Z, Vaziri A. Origami-inspired cellular metamaterial with anisotropic multi-stability. Adv Eng Mater 2019;21(2):1800895. https://doi.org/10.1002/adem.201800895.
[43] Filipov ET, Redoutey M. Mechanical characteristics of the bistable origami hypar. Extreme Mech Lett 2018;25:16–26. https://doi.org/10.1016/j.eml.2018.10.001.
[44] Chen Y, Yan J, Feng J. Geometric and kinematic analyses and novel characteristics of origami-inspired structures. Symmetry (Basel) 2019;11(9):1101. https://doi.org/10.3390/sym11091101.
[45] Feng H, Peng R, Zang S, Ma J, Chen Y. Rigid foldability and mountain-valley crease assignments of square-twist origami pattern. Mech Mach Theory 2020;152: 103947. https://doi.org/10.1016/j.mechmachtheory.2020.103947.
[46] Huffman. Curvature and creases: a primer on paper. IEEE Trans Comput 1976;25 (10):1010–9. https://doi.org/10.1109/TC.1976.1674542. 1.
[47] Wu W, You Z. Modelling rigid origami with quaternions and dual quaternions. Proc R Soc A 2010;466(2119):2155–74. https://doi.org/10.1098/rspa.2009.0625.
[48] Hayakawa K, Ohsaki M. Equilibrium path and stability analysis of rigid origami using energy minimization of frame model. Front Built Environ 2022;8:995710. https://doi.org/10.3389/fbuil.2022.995710.
[49] Li J, Chen Y, Feng X, Feng J, Sareh P. Computational modeling and energy absorption behavior of thin-walled tubes with the kresling origami pattern. J Int Assoc Shell Spat Struct 2021;62(2):71–81. https://doi.org/10.20898/j.iass.2021.008.
[50] Tao J, Li S. Asymmetric multi-stability from relaxing the rigid-folding conditions in a stacked Miura-ori cellular solid. Thin-Walled Struct 2022;179:109685. https://doi.org/10.1016/j.tws.2022.109685.
[51] Liu K, Tachi T, Paulino GH. Invariant and smooth limit of discrete geometry folded from bistable origami leading to multistable metasurfaces. Nat Commun 2019;10 (1):4238. https://doi.org/10.1038/s41467-019-11935-x.
[52] Cehula J, Prusa V. Computer modelling of origami-like structures made of light activated shape memory polymers. Int J Eng Sci 2020;150:103235. https://doi.org/10.1016/j.ijengsci.2020.103235.
[53] Hu YC, Zhou YX, Kwok KW, Sze KY. Simulating flexible origami structures by finite element method. Int J Mech Mater Des 2021;17(4):801–29. https://doi.org/10.1007/s10999-021-09538-w.
[54] Yuan T, Tang L, Liu Z, Liu J. Nonlinear dynamic formulation for flexible origami-based deployable structures considering self-contact and friction. Nonlinear Dyn 2021;106(3):1789–822. https://doi.org/10.1007/s11071-021-06860-y.
[55] Callens SJP, Zadpoor AA. From flat sheets to curved geometries: origami and kirigami approaches. Mater Today 2018;21(3):241–64. https://doi.org/10.1016/j.mattod.2017.10.004.
[56] Demaine ED, Demaine ML, Hart V, Price GN, Tachi T. Non)existence of pleated folds: how paper folds between creases. Graphs Combinat 2011;27(3):377–97. https://doi.org/10.1007/s00373-011-1025-2.
[57] Dias MA, Dudte LH, Mahadevan L, Santangelo CD. Geometric mechanics of curved crease origami. Phys Rev Lett 2012;109(11):114301. https://doi.org/10.1103/PhysRevLett.109.114301.
[58] Dias MA, Santangelo CD. The shape and mechanics of curved-fold origami structures. EPL 2012;100(5):54005. https://doi.org/10.1209/0295-5075/100/54005.
[59] Liu A, Johnson M, Sung C. Increasing reliability of self-folding of the origami hypar. J Mech Robot-Trans ASME 2022;14(6):60904. https://doi.org/10.1115/1.4054310.
[60] Alese L. Propagation of curved folding: the folded annulus with multiple creases exists. Beitr Algebra Geomet-Contrib Algebra Geom 2022;63(1):19–43. https://doi.org/10.1007/s13366-021-00568-1.
[61] Kumar P, Pellegrino S. Computation of kinematic paths and bifurcation points. Int J Solids Struct 2000;37(46):7003–27. https://doi.org/10.1016/S0020-7683(99)00327-3. 1.
[62] Chen Y, You Z. Two-fold symmetrical 6R foldable frame and its bifurcations. Int J Solids Struct 2009;46(25–26):4504–14. https://doi.org/10.1016/j.ijsolstr.2009.09.012.
[63] Chen Y, Sareh P, Yan J, Fallah AS, Feng J. An integrated geometric-graph-theoretic approach to representing origami structures and their corresponding truss frameworks. J Mech Des 2019;141(9):91402. https://doi.org/10.1115/1.4042791.
[64] Chen Y, Yan J, Feng J, Sareh P. Particle swarm optimization-based metaheuristic design generation of non-trivial flat-foldable origami tessellations with degree-4 vertices. J Mech Des 2020;143(1):11703. https://doi.org/10.1115/1.4047437.
[65] Chen Y, Lu C, Yan J, Feng J, Sareh P. Intelligent computational design of scalene-faceted flat-foldable tessellations. J Comput Des Eng 2022;9(5):1765–74. https://doi.org/10.1093/jcde/qwac082.

[66] Yu T, Hanna JA. Bifurcations of buckled, clamped anisotropic rods and thin bands under lateral end translations. J Mech Phys Solids 2019;122:657–85. https://doi.org/10.1016/j.jmps.2018.01.015.
[67] Huang W, Wang Y, Li X, Jawed MK. Shear induced supercritical pitchfork bifurcation of pre-buckled bands, from narrow strips to wide plates. J Mech Phys Solids 2020;145:104168. https://doi.org/10.1016/j.jmps.2020.104168.
[68] Healey TJ. A group-theoretic approach to computational bifurcation problems with symmetry. Comput Methods Appl Mech Eng 1988;67(3):257–95. https://doi.org/10.1016/0045-7825(88)90049-7.
[69] Wohlever JC, Healey TJ. A group theoretic approach to the global bifurcation analysis of an axially compressed cylindrical shell. Comput Methods Appl Mech Eng 1995;122(3–4):315–49. https://doi.org/10.1016/0045-7825(94)00734-5.
[70] Kaveh A, Nikbakht M. Improved group-theoretical method for eigenvalue problems of special symmetric structures, using graph theory. Adv Eng Softw 2010;41(1):22–31. https://doi.org/10.1016/j.advengsoft.2008.12.003.
[71] Guest SD, Fowler PW. Symmetry conditions and finite mechanisms. J Mech Mater Struct 2007;2(2):293–302. https://doi.org/10.2140/jomms.2007.2.293. edselc.2-52.0-34548542010.
[72] Chen Y, Feng J, Sun Q. Lower-order symmetric mechanism modes and bifurcation behavior of deployable bar structures with cyclic symmetry. Int J Solids Struct 2018;139:1–14. https://doi.org/10.1016/j.ijsolstr.2017.05.008.
[73] Chen Y, Sun Q, Feng J. Group-theoretical form-finding of cable-strut structures based on irreducible representations for rigid-body translations. Int J Mech Sci 2018;144:205–15. https://doi.org/10.1016/j.ijmecsci.2018.05.057.
[74] Sareh P. The least symmetric crystallographic derivative of the developable double corrugation surface: Computational design using underlying conic and cubic curves. Mater Des. 2019;183:108128.
[75] Sareh P, Chen Y. Intrinsic non-flat-foldability of two-tile DDC surfaces composed of glide-reflected irregular quadrilaterals. nt J Mech Sci. 2020;185:105881.
[76] Sareh P, Guest SD. A framework for the symmetric generalisation of the Miura-ori. Int J Space Struct. 2015;30(2):141–52.
[77] Filipov ET, Liu K, Tachi T, Schenk M, Paulino GH. Bar and hinge models for scalable analysis of origami. Int J Solids Struct 2017;124:26–45. https://doi.org/10.1016/j.ijsolstr.2017.05.028.
[78] Liu K, Paulino GH. Nonlinear mechanics of non-rigid origami: an efficient computational approach. Proc R Soc A 2017;473(2206):20170348. https://doi.org/10.1098/rspa.2017.0348.
[79] Zingoni A. Group-theoretic exploitations of symmetry in computational solid and structural mechanics. Int J Numer Methods Eng 2009;79(3):253–89. https://doi.org/10.1002/nme.2576.
[80] Zingoni A. On the best choice of symmetry group for group-theoretic computational schemes in solid and structural mechanics. Comput Struct 2019;223:106101. https://doi.org/10.1016/j.compstruc.2019.106101.
[81] Ikeda K, Murota K. Bifurcation analysis of symmetric structures using block-diagonalization. Comput Methods Appl Mech Eng 1991;86(2):215–43. https://doi.org/10.1016/0045-7825(91)90128-S.
[82] Chen Y, Sareh P, Feng J, Sun Q. A computational method for automated detection of engineering structures with cyclic symmetries. Comput Struct 2017;191:153–64. https://doi.org/10.1016/j.compstruc.2017.06.013.
[83] Chen Y, Feng J. Generalized eigenvalue analysis of symmetric prestressed structures using group theory. J Comput Civil Eng 2012;26(4):488–97. https://doi.org/10.1061/(ASCE)CP.1943-5487.0000151. 1.
[84] Chen Y, Fan L, Bai Y, Feng J, Sareh P. Assigning mountain-valley fold lines of flat-foldable origami patterns based on graph theory and mixed-integer linear programming. Comput Struct 2020;239:106328. https://doi.org/10.1016/j.compstruc.2020.106328.
[85] Zhang P, Fan W, Chen Y, Feng J, Sareh P. Structural symmetry recognition in planar structures using convolutional neural networks. Eng Struct 2022;260:114227. https://doi.org/10.1016/j.engstruct.2022.114227.
[86] Lyu S, Qin B, Deng H, Ding X. Origami-based cellular mechanical metamaterials with tunable Poisson's ratio: construction and analysis. Int J Mech Sci 2021;212:106791. https://doi.org/10.1016/j.ijmecsci.2021.106791.
[87] Jalali E, Soltanizadeh H, Chen Y, Xie YM, Sareh P. Selective hinge removal strategy for architecting hierarchical auxetic metamaterials. Commun Mater 2022;3(1):97. https://doi.org/10.1038/s43246-022-00322-7.